Radboud Repository

Radboud University Nijmegen

PDF hosted at the Radboud Repository of the Radboud University Nijmegen

The following full text is a publisher's version.

For additional information about this publication click this link.
http://hdl.handle.net/2066/22724

Please be advised that this information was generated on 2017-12-05 and may be subject to change.

Physical characteristics of a commercial electronic portal imaging device

V. G. M. Althof,[a] J. C. J. de Boer,[b] H. Huizenga,[c] J. C. Stroom, and A. G. Visser
Department of Clinical Physics, Dr. Daniel den Hoed Cancer Center, Groene Hilledijk 301, 3075 EA Rotterdam, The Netherlands

B. N. Swanenburg
Laboratory for Space Research (SRON), Sorbonnelaan 2, 3584 CA Urecht, The Netherlands

(Received 20 November 1994; resubmitted 28 November 1995; accepted for publication 7 August 1996)

An electronic portal imaging device (EPID) for use in radiotherapy with high energy photons has been under development since 1985 and has been in clinical use since 1988. The x-ray detector consists of a metal plate/fluorescent screen combination, which is monitored by a charge-coupled device (CCD)-camera. This paper discusses the physical quantities governing image quality. A model which describes the signal and noise propagation through the detector is presented. The predicted contrasts and signal-to-noise ratios are found to be in agreement with measurements based on the EPID images. Based on this agreement the visibility of low contrast structures in clinical images has been calculated with the model. Sufficient visibility of relevant structures (4–10 mm water-equivalent thickness) has been obtained down to a delivered dose of 4 cGy at dose maximum. It is found that the described system is not limited by quantum noise but by camera read-out noise. In addition we predict that with a new type of CCD sensor the signal-to-noise ratio can be increased by a factor of 5 at small doses, enabling high quality imaging, for most relevant clinical situations, with a patient dose smaller than 4 cGy. The latter system would be quantum noise limited. © *1996 American Association of Physicists in Medicine.*

Key words: fluoroscopic portal imaging system, on-line portal imaging, radiotherapy verification, portal image quality

I. INTRODUCTION

Radiotherapy imaging in routine patient treatment during external irradiation with high energy photons is gradually becoming standard practice, both for quality assurance of field alignment, as well as to obtain documentation of the actual radiation treatments given. Low subject contrast, due to the small differential attenuation between various tissues at high energies, and unsharpness, due to (Compton) scattering in the detector itself and patient movement during the relatively long exposure times, are prominent characteristics of portal images.

The use of portal film as a treatment verification method has some distinct disadvantages, due to (i) the fixed slope of the "characteristic curve" of the film (which is why contrast optimization is not possible) and (ii) the time consuming film processing. Also, fast, quantitative and reliable comparison of a portal and a reference image requires computer assistance, and therefore the availability of both images in digitized format. The use of portal film in such a comparison would require a digitization procedure for each exposed film.

Although various methods for improvement of portal film quality have been proposed,[1,2] the problems involved in fast (and possibly on-line) image comparison remain unsolved. Therefore, electronic portal imaging devices (EPIDs) have been developed during the past 10 years.[3–10]

In 1985, a project was initiated at the Dr. Daniel den Hoed Cancer Center (DDHCC) in Rotterdam to develop a fluoroscopic imaging system, in collaboration with the Laboratory for Space Research in Leiden and Philips Medical Systems Radiotherapy in Crawley, UK. The purpose of this project was to develop an EPID for verification of patient set-up in routine clinical use. Therefore, the first goal was to develop a system which should be able to resolve low contrast structures (typically $\leqslant 2\%$) and should acquire, process and display images within a few seconds.

In 1988 the prototype SRI-100 was installed in the DDHCC at a 6 MV linear accelerator (Philips SL 75-10). Some of the physical characteristics of the system and preliminary clinical experience have been published previously.[3,9,11]

In the present paper, a model is presented which describes the performance of a charge-coupled device (CCD)-based fluoroscopic EPID. The predicted performance of the present camera and the noise characteristics are compared with measurements obtained from images acquired with standard imaging procedures offered by the system. The model is used to derive predictions about possible system improvements.

II. SYSTEM DESCRIPTION

A. General design

A diagram of the imaging system is shown in Fig. 1. High energy radiation is transformed into visible light by a metal screen–fluorescent screen combination, indicated by the "detector" in Fig. 1. The visible light is reflected by two 45°

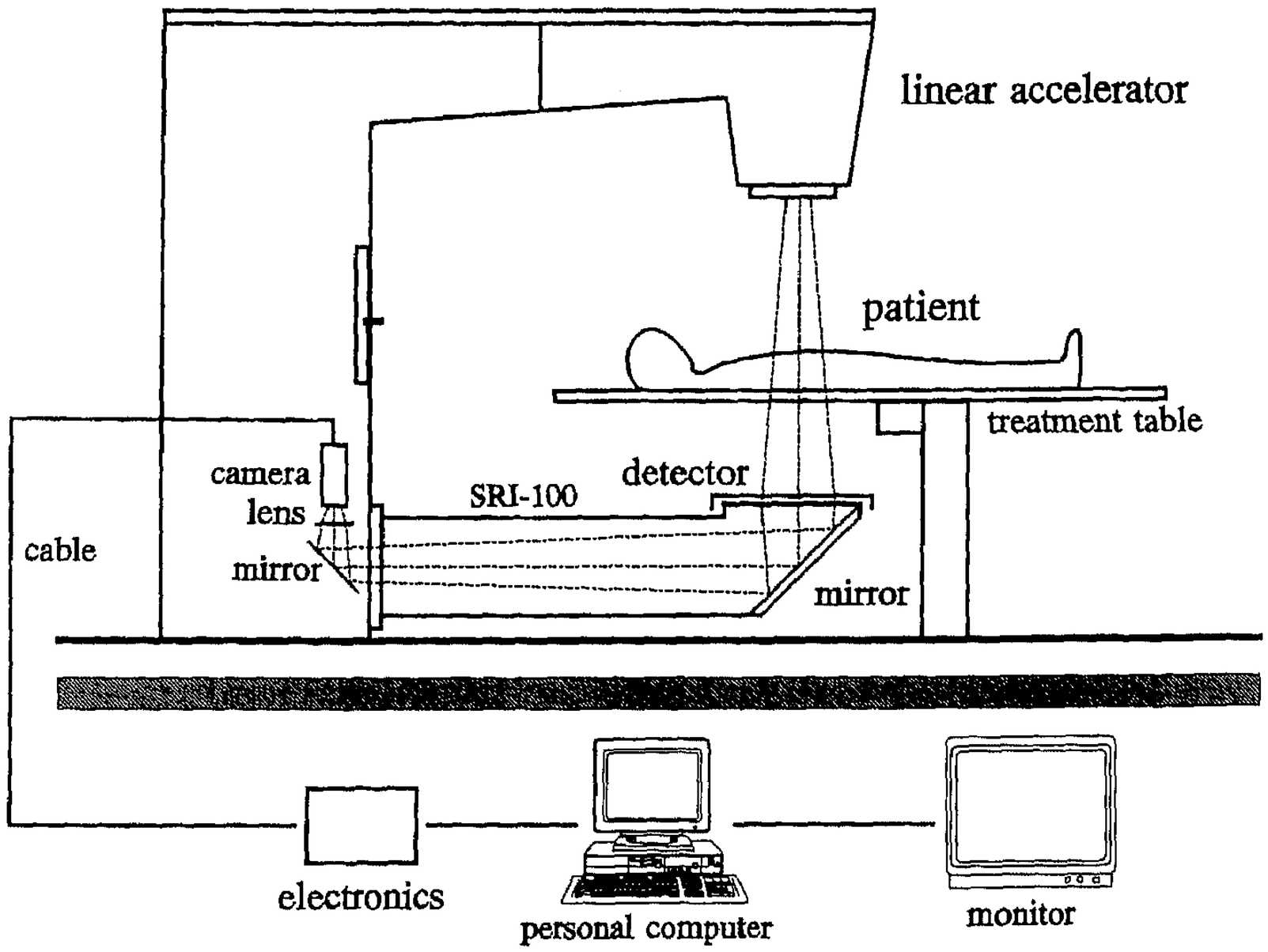

FIG. 1. A schematic diagram of the CCD based fluoroscopic electronic portal imaging system.

front-surface mirrors and collected by a large-aperture lens ($f/0.95$). The light is focused by the lens onto the light-sensitive sensor of a charge-coupled device (CCD) video camera (Adimec, previously HCS Vision Technology, type MX/CCD). The video signal from the camera is sampled in a slow-scan mode and digitized by an 8-bit AD converter (Data Translation DT2851 frame grabber), after it has been amplified and shifted by a software controlled gain and offset. Subsequent images are summed and processed via a 16-bit processor board (Data Translation DT2858 frame processor). For system configuration and process control, a parser command language is used, which enables the execution of user-defined initialization and imaging procedures.

B. Detector

The high energy photon detector consists of a 411 mg/cm^2 thick layer of Gd_2O_2S:Tb (gadolinium oxysulfide) glued to the back of a 1.5 mm stainless steel plate. The thickness of the stainless steel plate is close to the maximum dose depth at 6 MV, ensuring a nearly maximal energy deposit in the fluorescent layer as well as the absorption of scattered secondary electrons produced in the patient. The fluorescent screen emits visible light photons with a spectrum which peaks at 545 nm (near to the quantum efficiency peak at 580 nm of the CCD camera described below) when hit by electrons generated by the photon beam in the steel plate and the screen itself. The maximum field size covered by the screen 25×19 cm^2 at the isocenter, with a focus-isocenter distance of 100 cm and the focus-screen distance fixed at 160 cm.

The camera incorporates a CCD-sensor designed for standard video use in the interlaced read-out mode (see Table I). The sensor consists of 512×256 pixels and the pixel area is

TABLE I. Present system parameters.

Present system parameters	Symbol	Value	Unit
Dose at d_{max} (reference condition)	D	≥4	cGy or MU
Source axis distance	SAD	1000	mm
Depth of dose maximum	d_{max}	15	mm
Source to fluorescent screen distance	SFD	1600	mm
Mass surface density fluorescent screen	W_s	411	mg/cm^2
Efficiency of the fluorescent screen	η_s	0.20	···
Escape fraction	ξ	0.19	···
Energy fluorescent photons (545 nm)	E_s	3.64×10^{-19}	J
Lens transmission efficiency	τ	0.9	···
Demagnification factor	M	83.5	···
F-number of the lens	F	0.95	···
Quantum efficiency CCD-sensor	QE_c	0.14	···
Optical transmission seal window	f_c	1.0	···
Number of electrons generated in the CCD-sensor per MU [Eq. (5)]	S_e	89	μm^{-2} MU^{-1}
CCD-pixel area	A_c	156	μm^2
Read-out time (dead time)	t_d	0.08	s
Integration time at chip	t_f	0.08–1.2	s
Number of frames per signal	n_f	1–120	···
Dose rate	$\dot{D}$	340	MU/min
Signal from CCD-pixel [Eq. (6)] (t_f=0.24 s, n_f=1)	S_0/D	1.04×10^4	el./MU/pixel
Dark current uncooled camera	i_{dc}	20×10^3	el./s/pixel
Read out noise	N_r	80	el./frame/pixel
Digitization noise fraction	N_d	0.007	···
Signal-to-noise ratio, very short exposure (t_f=0.24, n_f=1)	S_0/N	72	···
Contrast increase per grey value	ϵ	0.002–0.02	···
Electrons per ADC unit	N_e	160	el./ADU

156 μm^2. Special electronics have been developed to integrate the signal at the sensor, in order to reduce the number of required frames for a given exposure. This will reduce the contribution of the read-out noise to the total noise (Sec. III B). Accumulation times, ranging from 80 ms to 1.2 s, can be set via the user interface. The system electronics restrict image accumulation to the odd fields of the interlaced video signal. The accumulation and read-out of the (unused) even fields is always 80 ms, and therefore introduces a dead time of 80 ms per frame.

C. Image acquisition

Images are acquired as follows. The accumulation time on the CCD-sensor, and the video signal offset and gain are controlled by software and are calculated from patient thickness, beam energy, wedge factor, target area and field size. The accumulation time of the CCD-sensor is maximized in such a fashion that the video signal can be brought within the signal range of the frame grabber using gain and offset, while avoiding saturation of the CCD. A number of video frames (calculated from dose required for the image and dose rate of the accelerator) is summed in a 16-bit frame processor. This reduces the noise and offers 16-bit resolution for further processing. A dark current image, which is acquired immediately before the portal image, is subtracted to correct for the signal due to thermal electrons. Non-uniformities in system response (e.g., originating in the fluorescent screen) are corrected by dividing the portal image by an open field calibration image. Such a calibration image is taken regularly (once a month). Finally, the portal image is displayed on a logarithmic grey scale (Sec. IV C).

III. THEORY OF SYSTEM PERFORMANCE

In this section a model is presented which describes the signal propagation through the detector as well as the causes and magnitude of the noise in the final image.

A. Theoretical derivation of signal levels

The fluence of optical photons, incident at the CCD-sensor, is related to the absorbed dose delivered to the fluorescent screen. Approximately, the dose D_s absorbed in the fluorescent screen is, via the inverse square law, related to the maximum dose D at depth $d_{\max}$ in a water tank positioned with the surface at the isocenter. Therefore,

$$D_s = \frac{D(\mathrm{SAD}+d_{\max})^2}{\mathrm{SFD}^2} \tag{1}$$

with SAD the source axis distance and SFD the source fluorescent screen distance. The dose D (in units of cGy) is generally equal to the number of accelerator Monitor Units (MU). Equation (1) neglects differences between energy deposition in a water phantom and in the metal plate/fluorescent screen combination, including differences in electron scattering and interface effects such as, for instance, build-down at the exit of the fluorescent screen.

The fluorescent screen emits optical photons of average energy E_s. The number of light photons emitted by the fluorescent screen per unit area, Φ_{ps}, is given by

$$\Phi_{ps} = \frac{D_s W_s \eta_s \xi_s}{E_s} \tag{2}$$

with W_s the mass surface density of the fluorescent screen, η_s the intrinsic x-ray to light energy conversion factor of the Gadolinium oxysulfide,[12] and ξ_s the fraction of optical photons which escapes from the screen.[13]

Only a small fraction of the emitted fluorescent photons will reach the CCD-sensor. The optical transport factor g_t (Ref. 14) is given by the light collection efficiency of the system, which is the ratio of the number of light quanta emitted by the fluorescent screen and the number collected via the video camera lens:

$$g_t = \frac{\tau}{4(1+M)^2 F^2} \tag{3}$$

with τ the lens transmission efficiency, M the ratio of the diameter of the fluorescent screen and the corresponding diameter at the CCD-sensor and F the F-number of the lens (focal length/diaphragm diameter). The factor 4 in the above equation stems from the Lambertian nature of the phosphor screen emission.[13]

The light is focused onto the CCD-sensor and the photon fluence incident on the CCD-chip ($\Phi_{ps} M^2 g_t$) produces an electron fluence Φ_{ec}, which depends on the quantum efficiency QE_c of the CCD-sensor and the attenuation f_c by the CCD seal window:

$$\Phi_{ec} = \Phi_{ps} M^2 g_t \mathrm{QE}_c f_c . \tag{4}$$

Hereafter, we will denote fluences for an unobstructed beam by the subscript "o" ("open field"). The number of electrons generated in a CCD-pixel for an open field, $S_{o,ec}$, follows from Φ_{ec} and the pixel area A_c. Since part of the dose is delivered during the dead time of the system, a correction factor equal to $t_f/(t_f+t_d)$ must be applied, with t_f the accumulation time and t_d the dead time. The signal, expressed in electrons per pixel per x-ray dose, becomes:

$$\frac{S_{o,ec}}{D} = \frac{\Phi_{o,ec}}{D} A_c \frac{t_f}{t_f+t_d}. \tag{5}$$

The average signal with an absorber present will be denoted by S_{ec}. The signal S_{ec} is represented by $S_{o,ec}$ multiplied by a correction factor which depends on the field size, beam energy, wedge factor, and water-equivalent absorber depth, as described in Sec. IV A.

B. Theoretical derivation of noise levels

The statistical noise component in a signal is mainly determined by the smallest number of quanta produced along the detection sequence. In the present situation the two relevant quantities are Φ_{es}, the number of high energy electrons interacting in the fluorescent screen per unit area, and Φ_{ec}, the number of photon-electrons produced in the CCD-sensor per unit area.

The number of high energy electrons per unit area per unit of dose delivered to the fluorescent screen depends on the mass surface density W_s of the fluorescent screen and can be roughly estimated as follows. Assume that all energy is lost in first Compton scattering, and that the energy lost is roughly one-third of the mean high energy x-ray photon, i.e., about one-tenth of the nominal x-ray beam energy E_{nom}. Then, the relation between Compton electron fluence Φ_{es} and dose can be approximated by:

$$\Phi_{es} \approx \frac{D_s W_s}{0.1 E_{\mathrm{nom}}}. \tag{6}$$

Since the area of the screen which is projected on one CCD-pixel equals M^2 times the CCD-pixel area, the ratio R_Φ of photo-electrons (detected in one pixel) to Compton electrons, follows from Eqs. (4) and (6), and (for $M \gg 1$) is given by

$$R_\Phi = \frac{\Phi_{ec}}{\Phi_{es} M^2} \approx \frac{0.1 E_{\mathrm{nom}}}{E_s} \frac{\eta_s \xi \mathrm{QE}_c f_c \tau}{4F^2 (1+M)^2}. \tag{7}$$

In the present system, the ratio R_Φ is smaller than 0.1 (using parameters from Table I). Analysis of noise propagation through the detector[13] yields the following expression for the standard deviation σ_q on the signal:

$$\sigma_q^2 = S_{ec}(1 + [1+\delta] R_\Phi), \tag{8}$$

where S_{ec} is the integrated electron signal per pixel [see Eqs. (5) and (12)]. The term R_Φ describes the quantum noise introduced by the x-ray counting statistics. The quantity δ represents additional noise due to the distribution function of the number of optical photons created, and is nearly 1.[13] Substituting parameters we find $(1+\delta) R_\Phi \approx 0.1$, which indicates that the main contribution to the statistical noise stems from the photo-electrons Poisson noise.

Another component of the noise is due to dark current. Dark current is generated continuously in the CCD-camera, also in the absence of any incident photon fluence. Thus, the number of electrons detected is higher than S_{ec}. To correct for this effect, a dark current signal is subtracted. The dark current image used in this subtraction, which features Poisson noise, is created during accumulation of n_{dc} separate dark current frames, acquired immediately before acquisition of the portal image. If the portal image is accumulated over n_f frames, the dark current image will be multiplied by a normalization factor n_f/n_{dc} before subtraction. The variance in the signal due to dark current in the corrected portal image can be found by adding, in quadrature, the Poisson noise in the normalized dark current image and the Poisson noise due to dark current in the uncorrected portal image:

$$\sigma_{dc}^2 = i_{dc} t_f n_f (1 + n_f/n_{dc}), \tag{9}$$

where i_{dc} is the dark current in electrons per second per pixel.

Also read-out noise contributes to the total noise. This is the noise associated with the output stages and the sampling circuits of the CCD. Therefore, each read-out of the CCD introduces a given amount of noise. The noise is expressed by the number N_r in units of electrons per read-out. For the method of determination of N_r, see Sec. IV B. Similar to the derivation of Eq. (9) we find that the variance due to read-out noise of n_f image frames corrected for dark current equals:

$$\sigma_r^2 = N_r^2 n_f (1 + n_f/n_{dc}). \tag{10}$$

The analog-digital conversion, occurring for each read-out, is another source of noise. This digitization noise is equivalent to $1/\sqrt{12}$ ADC unit (ADU).[15] A slightly larger value (half an ADU) is assumed to account for differential non-linearities in the frame grabber and additional digitization noise in the logarithmic compression. In clinical practice the mean signal will be above ADU 70 of the frame grabber. Therefore, a conservative estimate for the digitization noise is 0.7%. The variance in the signal due to digitization noise is approximated by:

$$\sigma_d^2 = n_f \{N_d (S_{ec}/n_f + i_{dc} t_f)\}^2 \tag{11}$$

with N_d the digitization noise fraction (0.007).

The correction for non-uniformities by an open field calibration image adds noise, but due to the full x-ray intensity in the calibration image and the larger imaging time applied for this image, this noise contribution is relatively small. The noise components in the flat field calibration image can be calculated also using Eqs. (8)–(11), and can simply be added to the variance components in the portal image to get the total variance. The noise contribution of the calibration image has been included in all calculations presented in this paper.

Finally, some noise is due to direct hits of CCD-pixels by indirect radiation, scattered via the environment, e.g., room walls. The magnitude depends on the shielding design of the CCD-sensor. The nature of this noise component yields a wide distribution of signal levels for a small fraction of the pixels. For each pixel the total amplitude does not increase with exposure time, but the number of affected pixels does. In our case this noise component is negligible due to the shielding design of the camera.

The mentioned noise components are statistically independent, so the variance of the total noise σ_{ec}^2 is equal to the summed variances of the noise components as given by Eqs. (8)–(11). The signal-to-noise ratio then becomes $\mathrm{SNR} = S_{ec}/\sigma_{ec}$.

IV. METHODS

A. Signal attenuation

To predict the signal for an attenuated beam, a semi-empirical method is applied. The EPID signal (S_{ec}) at the field center from a beam incident on a water phantom has been investigated at four energies (6 MV, 8 MV, 17 MV, 25 MV), a range of absorber depths (0–30 cm water), and a range of field sizes (5^2–25^2 cm^2). The focus-surface distance was 100 cm, the focus-detector distance was 160 cm. The water phantom was large enough to cover the largest field. Portal images were acquired with 42 monitor units. Signal

levels were normalized to the average dose rate during each exposure, which was measured using the dose rate monitor of the accelerator.

It was found that a simple relation describes the EPID signal adequately:

$$S_{ec}=S_{0,ec}F_w e^{\{i_F(F-25)-(\alpha_0+\alpha_F F)l\}} \tag{12}$$

in which F is the square root of the field area, F_w the wedge factor, and l the water depth. The signal $S_{0,ec}$ is defined for a 25^2 cm^2 square field size and zero absorber depth [defined in the model by Eq. (5)]. For each accelerator energy, the parameters α_0 (linear attenuation coefficient), α_F (linear attenuation correction, which describes the contribution to the signal from scatter in the absorber) and i_F (scatter contribution from the detector) can be obtained from four intensity measurements with two different beam sizes (7^2 and 25^2 cm^2) and two water phantom thicknesses (0 and 20 cm).

To predict the EPID signal behind an object emerged in water, Eq. (12) is applied, with l substituted by l_{eff}, which equals $\int \rho(l')dl'$ (ρ is the electron density relative to water and l' measures the depth along a beam ray line through the center of the object). This prediction is an approximation; it neglects the geometrical difference—and thus the difference in scatter effects[16,17]—between the addition of a layer of absorber material and the addition of a (small) object. Therefore it will only be valid in the case of $l_{\text{eff}} \approx l$, i.e., for low contrast objects.

B. Signal to ADU conversion

Results of measurements from the digitized image are given in pixel grey values which we need to convert to electrons per pixel. To find the relation between ADC output k and input signal S_{ec}, the number of electrons per ADU (N_e) must be determined ($k=S_{ec}N_e^{-1}$). N_e is defined for a reference signal gain g_{ref} which implies that for an arbitrary gain g, $k=(g/g_{\text{ref}})S_{ec}N_e^{-1}$.

The value of N_e is derived according to the "mean-variance" method, as described by Sims and Denton.[18] This method is based on the fact that, for fixed acquisition parameters, and in the absence of "fixed pattern noise" (offsets and gain differences per pixel in the detection chain and inhomogeneity of illumination) the variance of the image grey values will be a linear function of the image intensity (due to Poisson statistics). It is straightforward to show that the slope of this line equals $1/N_e$.[18]

In order to eliminate the contribution of fixed pattern noise we used an image which is obtained by subtraction of two images (obtained under identical illumination conditions) to derive the variance from. Plotting this variance (which describes read-out noise, digitization noise and quantum noise) against the mean of the input images should yield a line with a slope equal to $2/N_e$. It can be shown that this subtraction method should work even for large inhomogeneities in illumination over the CCD due to the properties of the Poisson noise, as long as the light field presented to the CCD while obtaining the two images is identical. However, homogeneity of illumination constrains the spread of values around the expected line.

In our experiment the CCD-sensor was illuminated by a light emitting diode (LED) placed in a lens cap behind a piece of frosted glass. The cap was placed over the lens with the camera focused at infinity. The LED current was varied using a multiturn potentiometer. The central 100×100 pixels were selected for analysis and the intensity variation from minimum to maximum grey level was less than 10% relative to the average grey level. During these measurements, care was taken that the signal levels were about equal to those found in clinical practice. Because the reference gain g_{ref} (and corresponding offset) was close to the nominal gain used during clinical imaging the linear response characterized by N_e should be applicable to the clinical situation.

The variance at zero signal is due to dark current noise, read-out noise and digitization noise. Since the dark current can be measured directly (see Sec. V D) and the digitization noise is known [Eq. (11)], the read-out noise N_r can be determined.

C. Image display

As mentioned, the grey values n in the clinical images displayed by the system are a logarithmic function of the signal. This relation is expressed by

$$n=-^{(1+\epsilon)}\log(S_{ec}/S_{ec,\max}) \approx -\frac{\ln(S_{ec}/S_{ec,\max})}{\epsilon} \tag{13}$$

with S_{ec} the signal from a specific CCD pixel, $S_{ec,\max}$ the expected maximum signal in the image, and $\epsilon \ll 1$. By adjusting the base of the logarithm $(1+\epsilon)$, the signal can be accommodated to the available display range in the 8-bit display buffer. The display range is the range of digitized signal levels selected for display at the video monitor. From Eq. (13) one directly infers that the display range R satisfies

$$R=(1+\epsilon)^{255}=S_{ec,\max}/S_{ec,\min}, \tag{14}$$

where $S_{ec,\min}$ is the smallest signal in the portal image.

The value of ϵ is calculated by estimating the minimum and maximum signals from the absorber thickness, target area, beam energy, and field size, based on Eq. (12). This ensures that the system always displays a patient image with an optimal display range and thus with a maximum contrast. The values of R (chosen for a 6 MV beam) range from 1.66 for images of the pelvis ($\epsilon=0.002$) to 9.82 for the breast images ($\epsilon=0.009$). Note that the value of ϵ determines the slope of the characteristic curve of the image.

D. Signal contrast ratio

The signal contrast ratio C in an image can be defined as the relative difference of the subject signal S_{obj} and the background signal S_{bg}:

$$C=\frac{S_{\text{obj}}-S_{\text{bg}}}{S_{\text{bg}}}. \tag{15}$$

(Note that the indices ec have been omitted for readability.) The above expression is similar to to the definition of signal contrast ratio given by Motz and Danos[16] in the case of low contrast structures. Equation (15), combined with Eq. (13) yields

$$C=(1+\epsilon)^{\Delta n}-1 \tag{16}$$

with $\Delta n = n_{\mathrm{bg}} - n_{\mathrm{obj}}$ the difference of background and object signal in grey levels in the digital image. The contrast corresponding to one grey value step is thus equal to ϵ.

E. Signal-to-noise ratio and contrast visibility

The noise in the background signal is denoted by σ_{bg}. The signal-to-noise ratio SNR can be derived from the image, similar to the derivation of Eq. (16), by determining the standard deviation σ_n, in grey levels, of the pixel value distribution in a representative region where only the background signal is present:

$$\mathrm{SNR}=\frac{S_{\mathrm{bg}}}{\sigma_{\mathrm{bg}}}\approx\frac{1}{\epsilon\sigma_n}. \tag{17}$$

The visibility of structures is directly related to the SNR of an image. In general, an object can be discerned if it generates a contrast larger than the threshold contrast C_{th}, which satisfies[19]

$$C_{\mathrm{th}}=\frac{5}{\mathrm{SNR}}. \tag{18}$$

The number 5 in the above equation is an average from values in literature which range from 3 to 7.[20–23] Because real objects viewed by the imager extend over several pixels, the SNR to be applied in formula (18) is larger than the ''single pixel'' SNR as the eye averages out noise for large image areas. In general one finds that objects of diameter d (measured in a plane parallel to the detector plane) become discernible if their contrast C satisfies $C \geqslant C_{\mathrm{th}}(d)=\kappa(d)/\mathrm{SNR}$ where the function $\kappa(d)$ is usually designated as the ''contrast-detail'' curve[23–25] and SNR refers to the SNR per pixel, as defined by Eq. (17). The quantity $\kappa(d)$ incorporates the above mentioned averaging of noise as well as spatial resolution characteristics of the imager. In general, $\kappa(d)$ varies slowly for $d \gg$ the resolution of the system.[26]

With measurements described in Sec. V E in hindsight, we define the contrast visibility $L_v(d)$ as the minimum water-equivalent thickness of an object of diameter d which renders it visible in an image. The value of d is the diameter at isocenter distance back projected along the beam ray lines, which is usually no more than a 20% correction to the true diameter. Because $C_{\mathrm{th}}(d) \approx \alpha L_v(d)$, where $\alpha=\alpha_0+\alpha_F F$ (see Sec. IV A) is the effective linear attenuation coefficient, we derive from the above that the contrast visibility must satisfy:

$$L_v(d)=\frac{\kappa(d)}{\alpha\mathrm{SNR}}. \tag{19}$$

A low contrast phantom[19] has been used to test the system's capability of detecting low contrast structures and to verify the prediction of contrast ratios and SNR values. The phantom was also used to determine the value of κ in Eq. (19). The phantom consists of 13 cylindrical PVD rods ($\rho=1.271$) of various heights (5 mm to 26 mm) and 1.6 cm diameter, placed in a circle. The center of this phantom was placed at the isocenter. In air, the effective thickness of the rods (l_ρ) ranges from 6.4 to 33 mm. When the rods are emerged in water, the effective thickness ($l(\rho-1)$) ranges from 1.4 to 7.0 mm.

TABLE II. Typical values for the parameters a_0, a_F, and i_F describing the attenuation of the signal as function of field size, absorber depth and energy.

Energy (MV)	α_0 ($L=7$ cm) [cm^{-1}]	α_F [cm^{-2}]	i_F [cm^{-1}]
6	0.0494	-5.0×10^{-4}	1.5×10^{-2}
8	0.036	-3.5×10^{-4}	1.5×10^{-2}
17	0.031	-3.7×10^{-4}	1.5×10^{-2}
25	0.033	-5.4×10^{-4}	2.2×10^{-2}

V. RESULTS

In this section performance results are presented and compared to the model predictions. The relevant model parameters are listed in Table I.

A. Signal attenuation

The attenuation of the unobstructed beam by an absorber has been measured and parametrized as described in Sec. IV A. Typical values for the parameters are given in Table II (see also Sec. V E for a discussion of the attenuation coefficient α). The dependence of the CCD signal S_{ec} on the field size is larger than the dependence of the central axis dose at $d_{\max}$ on the field size. This effect is attributed to light backscattered from the mirror in a rather uniform fashion and cross-talk in the CCD-chip at a very low level.

B. Signal to ADU conversion

N_e has been determined experimentally according to the method described in Sec. IV B. A value of 160 electrons/ADU with a reproducibility better than 10% was found. In Fig. 2 half the variance of the difference of two input images is plotted against the mean of the input images for an accumulation time of 0.56 s. The slope of the line yields $1/N_e$ (Sec. IV B).

The origin of the horizontal axis was normalized in this figure so as to correspond to zero signal. Therefore, the variance at zero average grey value should consist of read-out noise and digitization noise. If one takes into account a variance of 1/12 channel for the latter, a read-out noise $N_r=80$ electrons/frame/pixel is found.

C. Signal level

The value of $S_{o,ec}/D$ in units of photo-electrons per pixel per monitor unit, was determined by both experiment and calculation. The measured value is obtained by converting the measured signal in ADU to photo-electrons using the

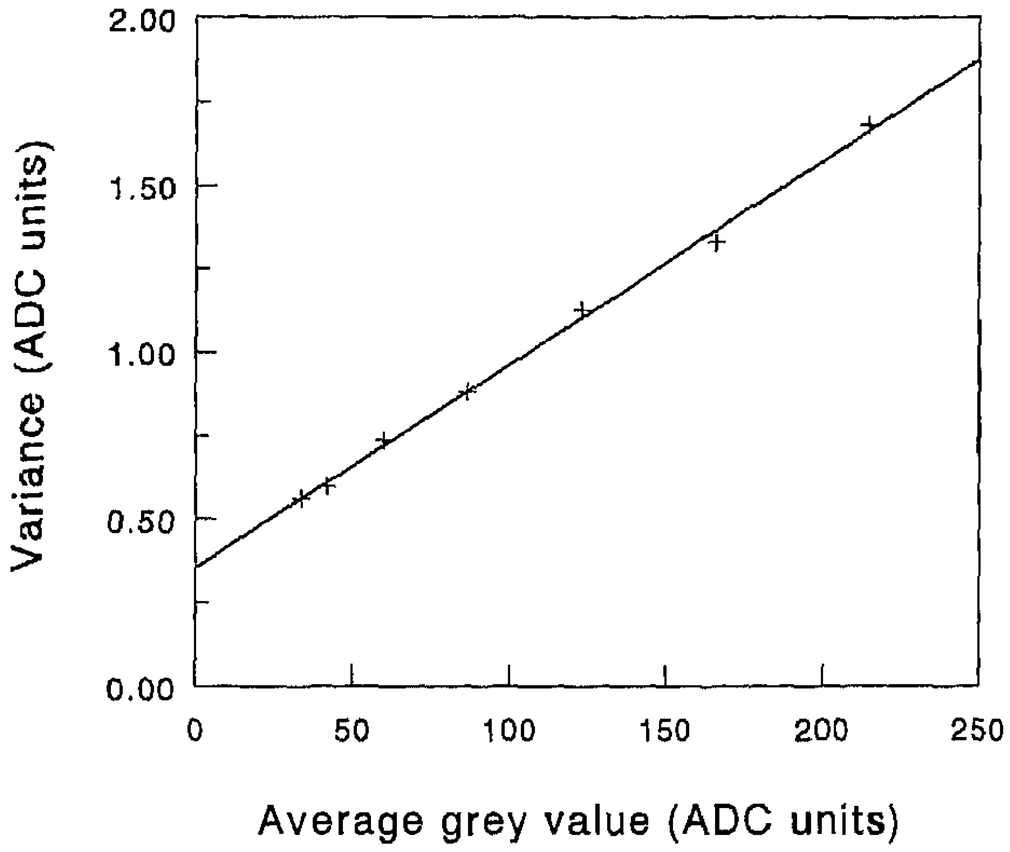

FIG. 2. Variance/2 of measured grey values in the difference of two images obtained at the standard gain as a function of the average grey value in the input images. The slope of the line fit is $1/N_e$.

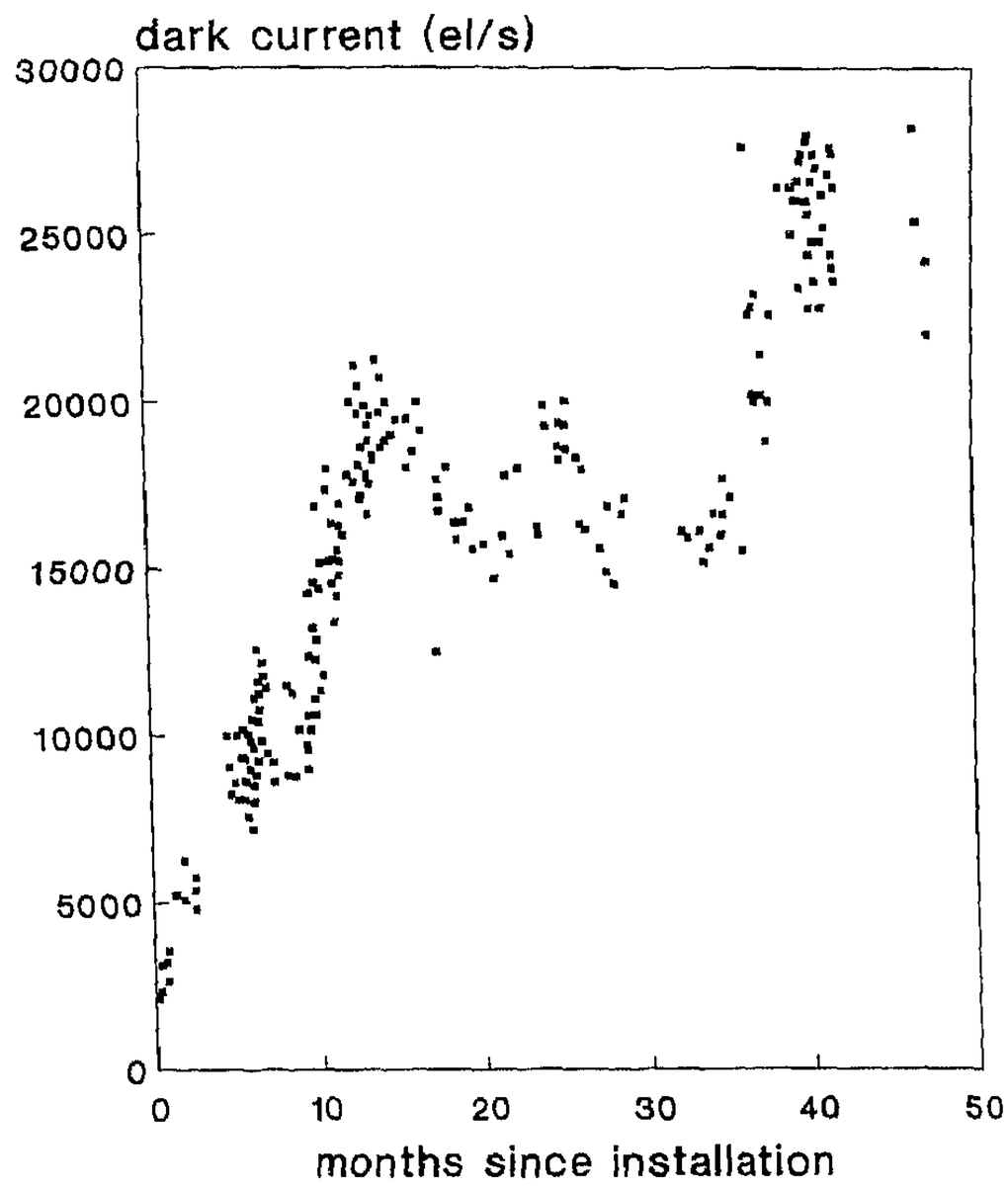

FIG. 3. Variation in dark current over the 4 years since installation of the (non-Peltier cooled) system in July 1988.

experimentally determined value of N_e (Sec. V B). For an integration time at the CCD-sensor of 0.24 s, $S_{o,ec}/D$ equals 1.0×10^4 el/MU. For longer integration times at the CCD-sensor, this number is larger due to the reduced influence of the dead time of the system, as can be seen from Eq. (5).

The signal $S_{o,ec}/D$ can also be calculated using Eq. (5). Inserting the present system parameters (as listed in Table I) a $S_{o,ec}/D$ value of 1.04×10^4 was obtained, in good agreement with the measured value. Therefore, although the values of η_s and QE_c are not precisely known, the use of the values $\eta_s=0.2$[12] and $QE_c=0.14$ (taken from specifications) seem to be valid. These parameter values are also within the expected range.[27]

D. Dark current behavior

Many sensitive chips such as CCDs show deterioration due to radiation damage at accumulated doses between 10 and 100 Gy. At first by generating more noise, mainly due to an increased dark current, and later by pixel defects. Based on TLD measurements at the CCD location we expect an accumulative dose per year of 1.3 Gy for a 2 cm thick lead camera shielding (assuming a dose of 10 kGy at the isocenter per year).

Dark current behavior has been monitored since installation. Figure 3 shows the variation in dark current (i_{dc}) over the first 4 years. The day-to-day scatter in the data is caused by temperature fluctuations: the temperature measured near the camera would vary up to 4 °C during the day whereas the dependence of the dark current on temperature was measured to be 8% per °C (in agreement with CCD specifications). In the first months after installation, when the system was not used frequently, the CCD-sensor was rather sensitive to radiation damage. Fifteen months after installation, it was decided to read out the CCD-sensor continuously, also when the system was not in use. This measure apparently resulted in a stabilization of the dark current level. Remaining fluctuations seem associated with seasonal variations. The steep increase after month 35 is not well understood.

At the time of acquisition of the images which were used to calculate SNR values (Sec. V F) the dark current was 2.1 $(\pm0.2)\times10^4$ el. s^{-1} $pixel^{-1}$. The dark current values during the "stable" period (month 15–35) are in the range $(1.5–2.2)\times10^4$ el. s^{-1} $pixel^{-1}$. In Table I we therefore list the typical value $i_{dc}=2\times10^4$ el. s^{-1} $pixel^{-1}$.

At present, the image quality (SNR ratio) is not seriously affected by the dark current due to the subtraction procedure described in Sec. II C. Although the dark current can rise to 30% of the image signal level (see Table I), the dynamic range is not significantly reduced due to the fact that an automatically calculated camera offset is applied to the video signal which keeps the mean dark current signal in the low range of the ADC. However, since the full dark current distribution over the image needs to be properly digitized in order to make subtraction feasible, an increasing dark current will ultimately deteriorate the image quality by limiting the dynamic range and by increasing the noise. Therefore, subsequent SRI-100 systems are carried out with a Peltier-cooled CCD-sensor. This reduces the dark current to approximately 1000 el. s^{-1} $pixel^{-1}$ which is small compared to the average signal.

E. Signal contrast ratio

In order to determine contrasts, images of the contrast phantom described in Sec. IV E were obtained with $\epsilon=0.002$ and doses of 4, 10, 30, and 100 MU (respectively $n_f=2$, 5, 16, and 40 frames, $n_{dc}=10$, $t_f=0.24$ s) for various water depths (Fig. 4). They were corrected (Sec. II C) using a flat

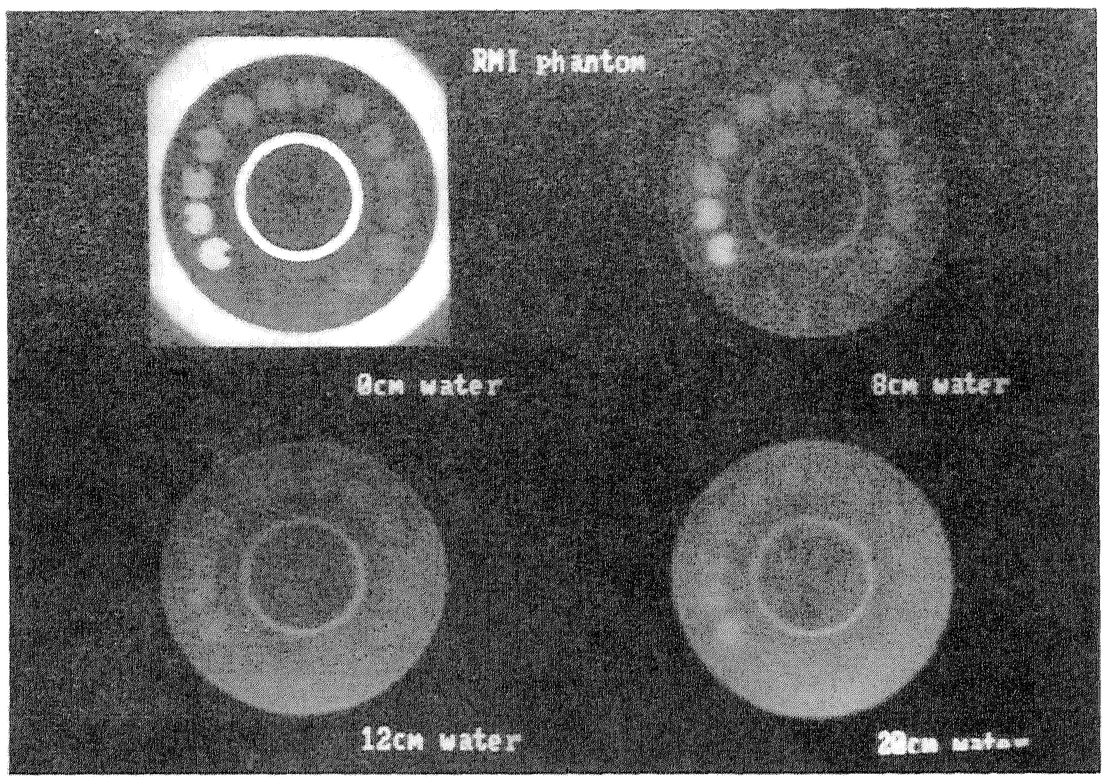

FIG. 4. Megavoltage images of the RMI-phantom at 6 MV, in air and with 8 cm, 12 cm, and 20 cm water.

field calibration image which was obtained for a 30^2 cm^2 square field ($n_f=24$, $n_{dc}=24$, $t_f=0.24$ s, $D=44$ MU).

A region (area >100 pixels) was selected on top of each PVC rod in the RMI phantom, and the mean grey value n_{obj} was measured. The background grey value n_{bg} was obtained from two regions close to each cylinder, one towards the center and one towards the outer boundary of the phantom (due to cylindrical symmetry, gradients will mainly run along the radial direction of the RMI phantom). Using Eq. (16) the measured differences, in grey levels, were transformed to signal contrast ratio values. Results for the rods in air and in 20 cm water, as determined from images acquired with 100 MU, are presented in Fig. 5. Evidently, the system shows a linear response of the signal contrast ratio as a function of object thickness.

The predicted signal contrast ratio for the rods in water was calculated according to Eqs. (12), (15), and Table II [since the PVC rods were emerged in 20 cm water, the ratio of object to background path length, l_{eff}/l (Sec. IV A) is in the range of 1.007–1.035, so we applied Eq. (12) to predict signal behind the rods]. The resulting curve is also shown in Fig. 5 (solid line). The least squares fit to the data (not shown) yields a (linear) attenuation coefficient of $\alpha=0.039 \pm 0.02$ (1 SD) cm^{-1}, consistent with the model value of $\alpha=\alpha_0+\alpha_F F=0.041$ cm^{-1} [see Eq. (12), all numbers apply to water-equivalent material].

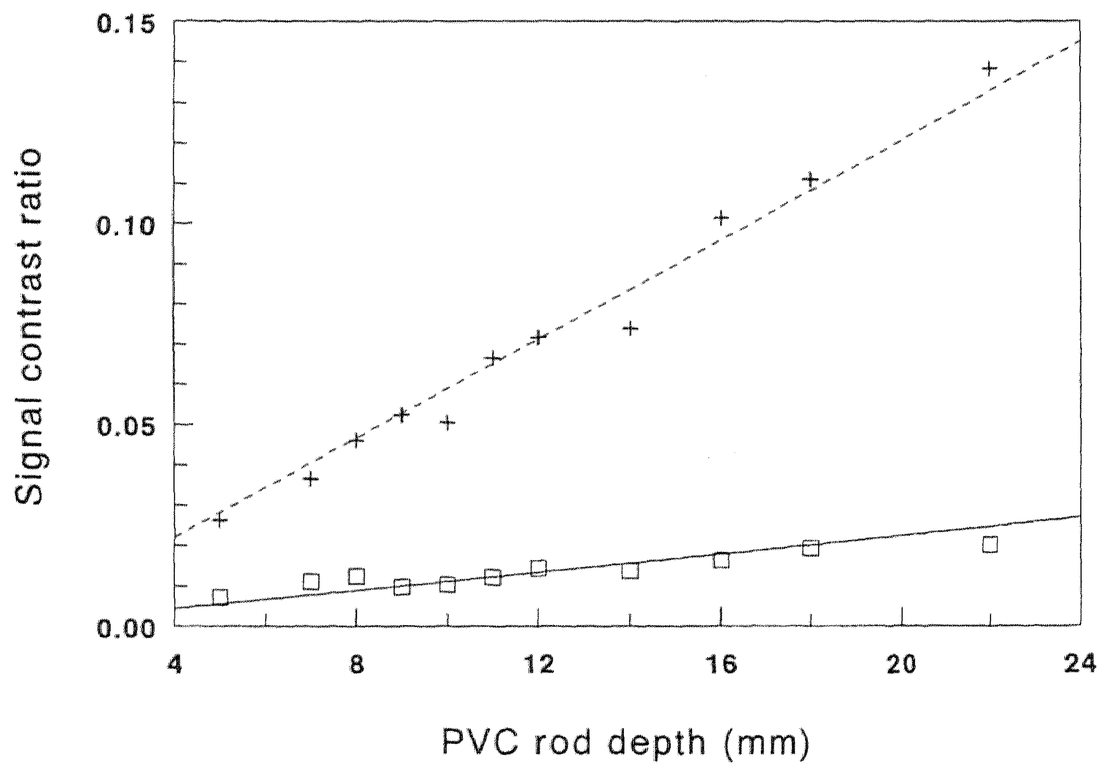

FIG. 5. Signal contrast ratios of PVC rods, measured for rods in air (+) and in 20 cm water (□). The closed line is the model prediction for rods in water. The dashed curve is the least squares fit to the rods in air data (see the text). The x-axis gives the geometrical thickness of the PVC rods in mm.

For the rods in air, the model does not make a proper prediction for the attenuation coefficient of the rods since Eq. (12) does not hold for a few objects of high density embedded in a medium of negligible density with most ray-lines passing only through air (see Sec. IV A). However, the value of α derived for the PVC rods in air must be bounded by the model values of (i) the attenuation for pure absorption (no scattering), or $\alpha=0.049$ and (ii) the attenuation which includes scattering for a homogeneous slab of material, i.e., $\alpha=0.041$ cm^{-1} like above. In fact, the fit depicted in Fig. 5 (dashed line) gives $\alpha=0.045\pm0.01$ cm^{-1}, consistent with these limits.

Note that the values of α derived from the rods in air and water are in the range 0.03–0.05 cm^{-1}, in agreement with the bounds posed by the x-ray attenuation coefficient in water (0.0494 cm^{-1}) and the x-ray absorption coefficient (0.0261 cm^{-1}),[28] both taken at the mean x-ray beam energy of 2 MeV.

F. Signal to noise ratio

Combining the results of Secs. V C and V E, we may conclude that absolute signal levels of the EPID can be well described as long as the absorber is fairly homogeneous over the area of the irradiation field. Based on this result, we verified the predictions for image noise by calculating and measuring the SNR for the same set of images used to derive the contrast ratio values.

The measurements in Fig. 6 were obtained by evaluating Eq. (17) for at least four nearby regions in each image which did not intersect the area of a PVC rod. The error bars are 2σ wide, where σ is the 1 SD error estimate based on the difference between the regions. As can be judged from Fig. 6, the agreement between measured and predicated SNR values is within the estimated errors.

For illustration we also show in Fig. 6 the SNR of the present system configuration for 20 cm of water equivalent absorber under the assumption that the quantum noise of the photo-electrons is the only noise source, taking into account the quantum noise in the flat field image (dashed curve). From a comparison of this curve to the measured data, it is apparent that the SRI-100 described in this paper has large contributions from noise sources other than quantum statistics. For the acquisition sequence of the images used for analysis (which is typical for a clinical acquisition) the readout noise is the dominant source of noise according to our calculations, and the more so at long exposures.

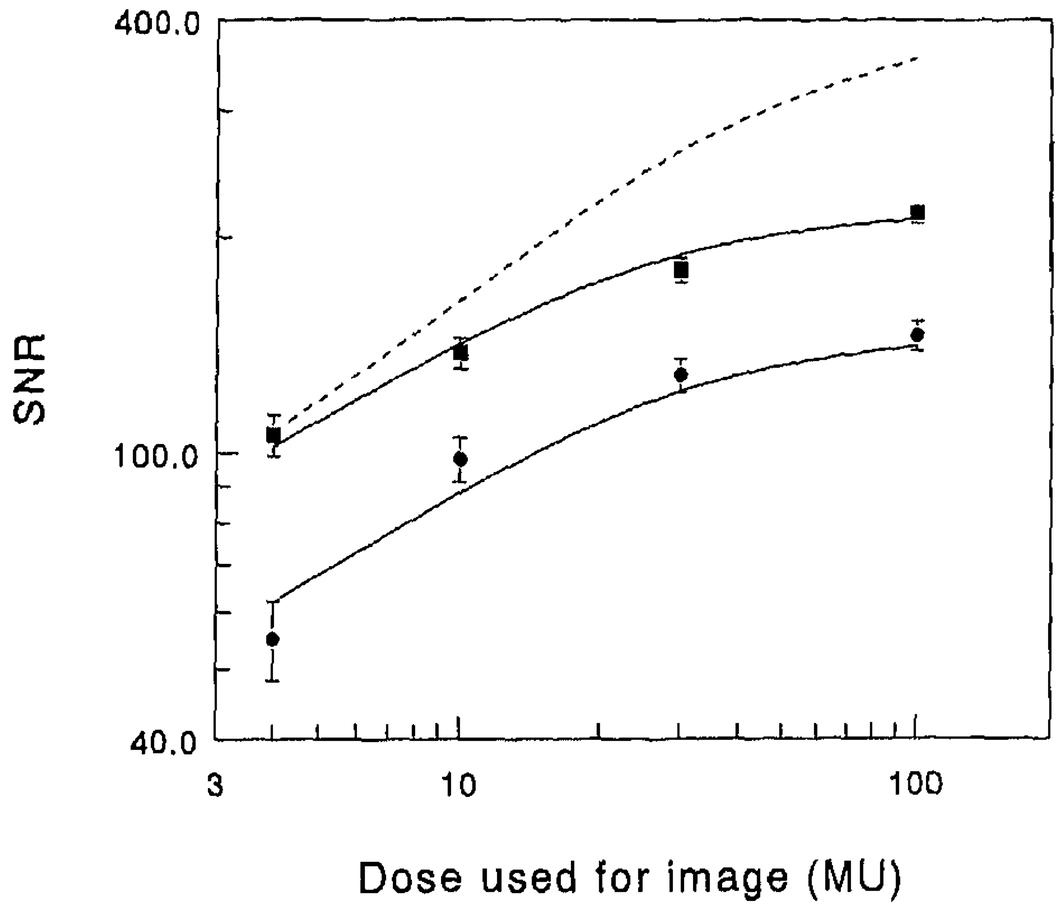

FIG. 6. Signal-to-noise ratio as measured in air (■) and in 20 cm water (●) and corresponding predictions (solid lines). If all detector noise would be removed, except for the photon and photo-electron quantum noise, the SNR curve given by the dashed line would apply in the case of 20 cm water equivalent absorber.

G. Contrast visibility

In order to determine contrast visibility as a function of SNR, we looked at low contrast features in the described phantom images for water. Applying Eq. (19) to these images, we find $\kappa=1.2\pm0.1$ for the PVC rods of 1.6 cm diameter in the image. Given the large number of pixels involved in the detection of one PVC rod, we expect that $\kappa(d>1-2$ cm) ≈ 1 so that we may predict the contrast visibility for large structures as $L_v \approx (\alpha\ \mathrm{SNR})^{-1}$. The latter expression for L_v is consistent with the results of an analysis of the visibility of structures in clinical portal images of pelvic fields.

From the attenuation coefficient α (Table II) and measured noise values we may now directly calculate the contrast visibility for large structures as a function of absorber thickness and dose. Table III summarizes the results. These calculations have been performed for the image acquisition parameters applied during clinical imaging. Obviously, in most practical cases structures of 4–10 mm water-equivalent path length (1–2 cm bone) will become visible in a 4 MU image. This makes it feasible to obtain a short exposure image and check the patient set-up before delivering the remaining dose (a procedure which is sometimes applied at our institute).

As expected, the visibility of structures decreases with increasing phantom thickness due to the decreasing SNR.

TABLE III. Contrast visibility, measured at 6 MV, in absorbers of various depths.

Absorber depth	100 mm	200 mm	300 mm	400 mm
Check exposure, 4 MU	3.1 mm	4.6 mm	7.2 mm	11.0 mm
Short exposure, 10 MU	1.9 mm	2.5 mm	3.6 mm	5.1 mm
Medium exposure, 30 MU	1.5 mm	1.9 mm	2.6 mm	3.7 mm
Long exposure, 100 MU	1.3 mm	1.6 mm	2.1 mm	2.9 mm

TABLE IV. Future system characteristics.

	Present system	Future system
Size CCD-sensor (cm^2)	0.204	3.5
Number of pixels	512×256	512×512
Pixel area (μm^2)	156	576
Quantum efficiency QE_e	0.14	0.30
Dark current i_{dc} (el./s/pixel)	2×10^4	0.1
Read-out noise N_r (el./frame/pixel)	80	20
Dead time t_d (s)	0.08	0.005
Digitization noise N_d	0.007	2×10^{-5}

One may compensate for this effect by increasing the exposure time. For a dose of 30 MU, L_v can be reduced to 4 mm for absorber thicknesses encountered in clinical practice.

VI. FUTURE SYSTEM PERFORMANCE

Development in CCD technology and image processing techniques are ongoing. CCD-sensors with larger light sensitive sensor areas and with 2048×2048 pixels are commercially available and are used for instance in space research technology. Also the quantum efficiency of back-illuminated CCD-sensors is significantly higher than the quantum efficiency of the CCD-sensor used at present. The present CCD features a rather high dark current, but new (so-called "multi-pinned phase") devices utilize a surface dark current reduction technique which, in combination with moderate cooling, reduces the dark current drastically. The current camera also has a large dead time of 80 ms per frame due to its special electronics (Sec. II B) which can be reduced to a few ms for current integrating frame transfer chips. Most slow-scan frame transfer chips do not yet achieve video rate read-out (50–60 frames/s) and are limited to about 2 frames/second (at least 0.5 s integration). Such low read-out rates are, however, effective in reducing the read-out noise.

We have selected a particular slow-scan frame transfer CCD (SITe S1502FA CCD), currently available, of which the characteristics are summarized in Table IV. This choice is a trade-off between good characteristics and read-out speed. If we apply the model outlined in Sec. II, inserting the parameters for such a camera and the other system parameters from Table I, we obtain the SNR (dashed) curves given in Fig. 7. The curves for 0 and 20 cm water absorber for the prototype SRI-100 system have also been shown for comparison (solid lines).

In calculating the dashed curves, we have assumed that the processing steps to reduce fixed pattern noise are the same as for the current prototype system. Also, the full well capacity of this camera has been taken into account to avoid saturation. The rather large read-out time of the 512×512 pixels (0.26 s at the maximum clock speed of 1 MHz) does in practice not introduce extra dead time: for an open field the chip does not saturate below an integration time of 0.44 s, so that during integration of a field, there is always sufficient time to read out the previous field. In order to fix the optics of the system, we have defined the size of a pixel,

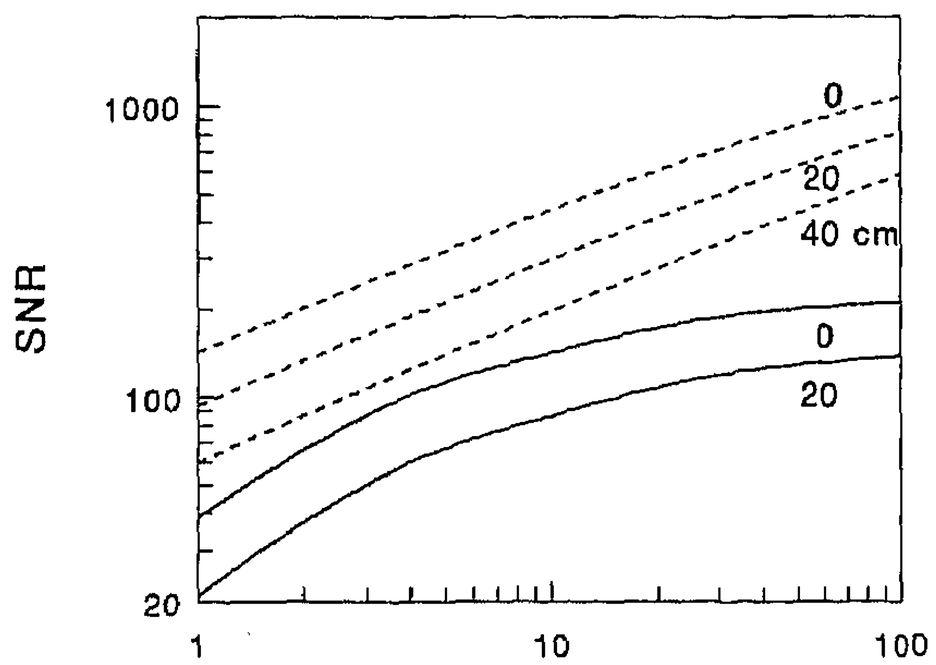

FIG. 7. SNR curves for an improved camera: dashed curves are for 0, 20, and 40 cm water equivalent absorber and a 15×15 cm^2 treatment field. Closed curves are for the prototype system for 0 and 20 cm absorber.

back projected to the fluorescent screen, to be equal to the corresponding size of a SRI-100 pixel in the horizontal direction (≈0.5 mm at isocenter).

The SNR curves for the new system are roughly linear on the log-log scale in the dose range of 0 to about 30 MU. This is because in this range the noise is now entirely dominated by quantum noise (camera noise negligible) and so SNR $\propto\sqrt{\text{dose}}$. For larger dose values, the curves increase less steeply, because the noise in the flat field image (obtained with a 100 MU dose) increases the random noise of the corrected image (dependent on absorber thickness).

The SNR for 40 cm water absorber thickness for the improved camera is larger than the SNR of the prototype system for 0 cm absorber for all exposure times. For 25 cm water and 1 MU of dose (0.18 exposure), the predicted SNR is 85, implying a contrast visibility L_v of about 3 mm, already sufficient for proper clinical images. In this case a 4 MU image would yield L_v=1.5 mm, implying that for most practical purposes imaging would become feasible with doses ≤4 MU.

The value of R_Φ [see Eq. (7)] would increase to 0.36 for the new system, implying that the noise introduced by the counting statistics of the Compton electrons interacting in the screen becomes important for a type of camera which meets the specifications of Table IV.

VII. CONCLUSIONS

A simple model has been developed to describe the characteristics of the SRI-100 CCD-camera based fluoroscopic EPID. The model provides an analysis of signal and noise propagation through the EPID. The signal and noise characteristics of the SRI-100 have been measured and are properly described by the model. In clinical practice, the images obtained with 4 MU display sufficient contrast to discern objects of 4–10 mm water-equivalent thickness emerged in 20–30 cm water absorber if their diameter >1 cm (back-projected to isocenter), e.g., bones of 1–2 cm thickness in a patient of 20–30 cm thickness. A large improvement in performance is expected from the use of a new type of CCD camera, which would enable clinical imaging with exposures in the range of 1–4 MU. Contrary to the current situation, the SNR of the latter system would be determined predominantly by quantum noise of both the CCD and the fluorescent detector plate.

ACKNOWLEDGMENTS

The EPID described in this paper has been developed in a collaboration between the Laboratory for Space Research (Leiden), the Dr. Daniel den Hoed Cancer Center (Rotterdam) and Philips Medical Systems Radiotherapy (Crawley, UK). Furthermore, the clinical implementation and evaluation of the system has been supported by grants (Nos. NKB DDHK 88-2, NKB 92-86) from the Dutch Cancer Society. The authors thank J. Tierolf, M. Kengen, J. Hol, and E. Philippus for valuable discussions during the development phase and evaluation of the system. J. Koffijberg, D. Binnekamp, C. L. C. Creutzberg, and M. de Hoog made valuable contributions to the clinical introduction of the system.

[a]Present address: Institute for Radiotherapy and Curietherapy, Deventer, The Netherlands.
[b]Author to whom reprint requests should be addressed.
[c]Present address: Institute of Radiotherapy, University of Nÿmegen, The Netherlands.

[1]R. Sephton, M. Green, and C. Fitzpatrick, "A new system for port films," Int. J. Radiat. Oncol. Biol. Phys. **16**, 251–258 (1989).
[2]H. Meertens, "Digital processing of high-energy photon beam images," Med. Phys. **12**, 111–113 (1985).
[3]V. G. M. Althof, C. L. Creutzberg, H. Huizenga, A. G. Visser, and B. N. Swanenburg, "On the clinical use and characteristics of the first Philips Radiotherapy imaging system," in *Proceedings of the 10th International Conference on the Use of Computers in Radiation Therapy*, edited by S. Hukku and P. S. Iyer (Sanjay Gandhi Post Graduate Institute of Medical Sciences, Lucknow, India, 1990), pp. 107–110.
[4]A. L. Boyer, L. Antonuk, A. Fenster, M. van Herk, H. Meertens, P. Munro, L. E. Reinstein, and J. Wong, "A review of electronic portal imaging devices (EPIDs)," Med. Phys. **19**, 1–16 (1992).
[5]M. van Herk and H. Meertens, "A matrix ionisation chamber imaging device for on-line patient setup verification during radiotherapy," Radiother. Oncol. **11**, 369–378 (1988).
[6]E. J. Morton, W. Swindell, D. G. Lewis, and P. M. Evans, "A linear array, scintillation crystal-photodiode detector for megavoltage imaging," Med. Phys. **18**, 681–691 (1991).
[7]P. Munro, J. A. Rawlinson, and A. Fenster, "A digital fluoroscopic imaging device for radiotherapy localization," Proc. SPIE **1090**, 321–329 (1989).
[8]S. Shalev, T. Lee, K. Leszczynski, S. Cosby, T. Chu, L. Reinstein, and A. Meek, "Video techniques for on-line portal imaging," Comput. Med. Imaging Graph. **13**, 217–226 (1989).
[9]A. G. Visser, H. Huizenga, V. G. M. Althof, and B. N. Swanenburg, "Performance of a prototype fluoroscopic radiotherapy imaging system," Int. J. Radiat. Oncol. Biol. Phys. **18**, 43–50 (1990).
[10]J. Wong, W. R. Binns, A. Y. Cheng, L. Y. Geer, J. W. Epstein, J. Klarmann, and J. A. Purdy, "On-line radiotherapy imaging with an array of fiber-optic image reducers," Int. J. Radiat. Oncol. Biol. Phys. **18**, 1477–1484 (1990).
[11]B. Heijmen, A. G. Visser, and H. Huizenga, "In vivo dose measurements using an electronic portal imaging device: A feasibility study," Abstract ESTRO, Malmö, 1992.
[12]G. E. Giakoumakis, C. D. Nocimos, and P. X. Sandilos, "Absolute efficiency of Gd_2O_2S:Tb screens under fluoroscopic conditions," Phys. Med. Biol. **34**, 673–678 (1989).
[13]T. Radcliffe, G. Barnea, B. Wowk, R. Rajapakshe, and S. Shalev, "Monte Carlo optimization of metal/phosphor screens at megavoltage energies," Med. Phys. **20**, 1161–1169 (1993).

[14]W. Swindell, "The lens coupling efficiency in megavoltage imaging," Med. Phys. **18**, 1152 (1991).
[15]P. F. Panter, *Modulation, Noise and Spectral Analysis* (McGraw-Hill, New York, 1965).
[16]J. W. Motz and M. Danos, "Image information content and patient exposure," Med. Phys. **5**, 8–22 (1978).
[17]W. Swindell, E. J. Morton, P. M. Evans, and D. G. Lewis, "The design of megavoltage projection imaging systems: Some theoretical aspects," Med. Phys. **18**, 855–866 (1991).
[18]G. R. Sims and M. Bonner Denton, "Characterisation of a charge-injection-device camera system as a multichannel spectroscopic detector," Opt. Eng. **26**, 1008–1019 (1987).
[19]W. R. Lutz and B. E. Bjarngard, "A test object for evaluation of portal films," Int. J. Radiat. Oncol. Biol. Phys. **11**, 631–634 (1985).
[20]A. Rose, "The sensitivity performance of the Human Eye on an Absolute Scale," J. Opt. Soc. Am. **38**, 196 (1948).
[21]L. Dong and A. L. Boyer, "An objective method for evaluating portal imaging devices," Med. Phys. **21**, 755–760 (1994).
[22]D. Rimkus and N. A. Baily, "Patient exposure requirements for high contrast resolution digital radiographic systems," Am. J. Roentgenol. **142**, 603–608 (1984).
[23]G. Cohen, L. K. Wagner, and S. R. Amtey, "Contrast-detail-dose and dose efficiency of a scanning digital and a screen-film-grid radiographic system," Med. Phys. **8**, 358–367 (1981).
[24]P. Munro and J. A. Rawlinson, "Therapy Imaging: A signal-to-noise analysis of a fluoroscopic imaging system for radiotherapy localization," Med. Phys. **17**, 763–772 (1990).
[25]S. Shalev, "Treatment verification using digital imaging," in *Radiation Therapy Physics*, edited by A. R. Smith (Springer, Berlin, 1995), pp. 155–173.
[26]B. H. Hasegawa, *The Physics of Medical X-ray Imaging* (Medical Physics, Madison, WI, 1991), 2nd ed.
[27]G. Zwieg and D. A. Zwieg, "Radioluminescent imaging: factors affecting total light output," Proc. SPIE **419**, 297–301 (1979).
[28]H. Hubbell, *Photon Cross Sections, Attenuation Coefficient and Energy Absorption Coefficients from 10 KeV to 100 GeV* (U.S.A. Department of Commerce, Washington, D.C., 1969), NSRDS-NBS No. 29.